JGP Journal of General Physiology

ARTICLE

Excitation–Contraction Coupling

Phosphorylation of RyR2 simultaneously expands the dyad and rearranges the tetramers

Parisa Asghari[1], David R.L. Scriven[1], Saba Shahrasebi[1], Hector H. Valdivia[2], Katherina M. Alsina[3], Carmen R. Valdivia[2], J. Alberto Navarro-Garcia[4], Xander H.T. Wehrens[4], and Edwin D.W. Moore[1]

We have previously demonstrated that type II ryanodine receptors (RyR2) tetramers can be rapidly rearranged in response to a phosphorylation cocktail. The cocktail modified downstream targets indiscriminately, making it impossible to determine whether phosphorylation of RyR2 was an essential element of the response. Here, we used the β-agonist isoproterenol and mice homozygous for one of the following clinically relevant mutations: S2030A, S2808A, S2814A, or S2814D. We measured the length of the dyad using transmission electron microscopy (TEM) and directly visualized RyR2 distribution using dual-tilt electron tomography. We found that the S2814D mutation, by itself, significantly expanded the dyad and reorganized the tetramers, suggesting a direct link between the phosphorylation state of the tetramer and its microarchitecture. S2808A and S2814A mutant mice, as well as wild types, had significant expansions of their dyads in response to isoproterenol, while S2030A mutants did not. In agreement with functional data from these mutants, S2030 and S2808 were necessary for a complete β-adrenergic response, unlike S2814 mutants. Additionally, all mutants had unique effects on the organization of their tetramer arrays. Lastly, the correlation of structural with functional changes suggests that tetramer–tetramer contacts play an important functional role. We thus conclude that both the size of the dyad and the arrangement of the tetramers are linked to the state of the channel tetramer and can be dynamically altered by a β-adrenergic receptor agonist.

Introduction

The type II ryanodine receptor (RyR2) is a large, 2.2 MDa, homotetrameric Ca^{2+}-activated Ca^{2+} ion channel located in the endoplasmic and sarcoplasmic reticulum of many cells (Lanner et al., 2010; Van Petegem, 2015; Meissner, 2017). In the heart, its distribution appears to be limited to the junctional sarcoplasmic reticulum (jSR), which in ventricular cardiomyocytes is located ∼15 nm distant from the sarcolemma and the transverse and axial t-tubules (Asghari et al., 2009). The close apposition of the adjacent membranes creates a space of restricted diffusion, the dyad, enabling the small current through $Ca_v1.2$ to activate the underlying RyR2 through Ca^{2+}-induced Ca^{2+} release (CICR) despite the tetramers' relatively low affinity for Ca^{2+} (Carl et al., 1995; Sun et al., 1995; Franzini-Armstrong, 2018). Each cell has thousands of dyads (Scriven et al., 2010), and in systole, the action potential coordinates their near-simultaneous release of Ca^{2+} into the myoplasm to produce a coordinated contraction.

In diastole, tetramers open stochastically, but with low probability (Cheng et al., 1993; Satoh et al., 1997). A single tetramer opening may result in an isolated event, a Ca^{2+} quark (Lipp and Niggli, 1996), but since tetramers can be distributed in clusters, some with several hundred members (Baddeley et al., 2009; Hayashi et al., 2009), inter-RyR2 CICR can result in larger Ca^{2+} release events, blips (Iaparov et al., 2021), or sparks (Cheng et al., 1993; López-López et al., 1994) depending on the number that is opened. Diastolic Ca^{2+} release, or leak, is normal but becomes dangerously elevated in many inherited and acquired cardiac diseases, such as catecholaminergic polymorphic ventricular tachycardia (CPVT) and heart failure (Keefe et al., 2023). This has led to increased morbidity and mortality (Bers, 2014), which is driving efforts to understand how RyR2 is regulated.

Intuitively, the microarchitecture of the dyad should affect the spatial and temporal characteristics of Ca^{2+} sparks and

[1]Department of Cellular and Physiological Sciences, Life Sciences Institute, University of British Columbia, Vancouver, Canada; [2]Department of Medicine, University of Wisconsin School of Medicine and Public Health, Madison, WI, USA; [3]Castle Biosciences Inc., Friendswood, TX, USA; [4]Department of Integrative Physiology, Cardiovascular Research Institute, Baylor College of Medicine, Houston, TX, USA.

Correspondence to Edwin D.W. Moore: edwin.moore@ubc.ca.

This work is part of a special issue on excitation–contraction coupling.

diastolic Ca^{2+} release, and this has been demonstrated by mathematical models which have highlighted the importance of the number of tetramers in a cluster, their relative positions, density, and coupling efficiency (Tanskanen et al., 2007; Cannell et al., 2013; Iaparov et al., 2019, 2021).

Direct examination of the tetramers' positions in intact rat and human myocyte dyads using electron tomography has shown that the array is irregular but neither random nor static (Asghari et al., 2014). At rest, most of the tetramers are in contact with at least one other in positions that were broadly characterized as side-by-side or checkerboard and in roughly comparable proportions. Factors that decreased the Ca^{2+} spark frequency, 4 mM Mg^{2+}, and the immunophilins FKBP12 and FKBP12.6, produced clusters with significantly more tetramers in the side-by-side configuration at the expense of those in a checkerboard while those that increased the Ca^{2+} spark frequency, 0.1 mM Mg^{2+}, and phosphorylation, did the opposite (Asghari et al., 2014, 2020). Under all experimental conditions, there were a few tetramers whose sides were not parallel to each other or were separated from their neighbors and were classified as isolated.

The correlated structure and function suggested a simple model in which the receptor's relative positions modify their gating parameters in some manner, with changes in the ratio of the checkerboard to side-by-side predicting changes in the Ca^{2+} spark frequency. An increase in the ratio is associated with an increase in spark frequency while the converse is also true. The simplest hypothesis, given experimental evidence (Marx et al., 2001; Porta et al., 2012), is that the increase in spark frequency in the checkerboard configuration might be due to positive allosteric interaction. Negative allosteric interaction in the side-by-side configuration is also possible but lacks experimental evidence. In this model, the mixed organization of checkerboard and side-by-side tetramers observed at rest in the fixed cells is a snapshot of a dynamic environment where the tetramers' relative positions are in motion, shifting with changes in their phosphorylation status, bound ions, and small molecules.

Our previous observations used permeabilized rat ventricular myocytes and a phosphorylation cocktail that activated numerous kinases while inhibiting phosphatases PP1 and PP2A (Asghari et al., 2014). This method produced indiscriminate phosphorylation of downstream targets, making it impossible to determine whether phosphorylation of RyR2 itself was required for tetramer rearrangement and, if so, which residues were involved. To investigate this, and to further investigate our model, we used well-characterized homozygous transgenic mice, S2808A$^{+/+}$ (Benkusky et al., 2007), S2814A$^{+/+}$ (Chelu et al., 2009), S2814D$^{+/+}$ (van Oort et al., 2010), and S2030A$^{+/+}$ (Potenza et al., 2019), which have generated functional data to which our structural analyses could be compared. The specific residues were selected because their phosphorylation has been implicated in the β-adrenergic "fight or flight" response in elevated diastolic Ca^{2+} leak and cardiac disease (Gaburjakova et al., 2020). S2808 and S2030 are phosphorylated by protein kinase A (PKA) and S2814 by calcium–calmodulin-dependent protein kinase II delta (CaMKIIδ) (Witcher et al., 1991; Marx et al., 2000; Wehrens et al., 2004; Xiao et al., 2005; Grimm et al., 2015; Potenza et al., 2019).

Mice were divided into groups whose hearts were perfused either with saline (control) or 300 nmol/liter isoproterenol (Iso). Given that RyR2 cluster sizes may be quickly altered by phosphorylation (Asghari et al., 2020), the length of close apposition between the jSR and the t-tubule or surface membrane, the dyad, was measured from 2-D transmission electron micrographs (Lavorato et al., 2015). The array's organization was examined using our well-established dual-tilt electron tomography acquisition and analysis techniques (Asghari et al., 2014, 2020).

The S2814D phosphomimetic mutant revealed a direct link between the state of the tetramer and the microarchitecture of the dyad, implying that phosphorylation of RyR2 itself initiates both an expansion of the dyad and a reorganization of the array, though the mechanisms are likely different. Iso produced the same structural changes in all of the WT mice and the S2808A and S2814A mutants, but not in the S2030A where the dyad did not expand and tetramer movement was crippled. All the mutants produced an abnormally large number of isolated tetramers indicating that each of the residues is important for maintaining intertetramer contact. The results showed that S2030 and S2808 are required for the normal β-adrenergic response, while S2814 is not. Using these same mouse models, published functional studies have supported these findings (van Oort et al., 2010; Respress et al., 2012; Ullrich et al., 2012; Potenza et al., 2019, 2020).

Materials and methods

The experiments used ventricular myocytes from 10–16-wk-old male C57BL/6J mice. Animal handling protocols were approved by the animal research care committees of the University of British Columbia, the University of Wisconsin, and Baylor College of Medicine and were in accordance with the guidelines of the Canadian Council on Animal Care as well as the Guide for the Care and Use of Laboratory Animals published by the US National Institutes of Health. Three hearts from each of RyR2-S2808A, RyR2-S2030A, and their wild type (WT) were from the laboratory of Dr. H.H. Valdivia (Benkusky et al., 2007; Potenza et al., 2019), and three hearts from each of RyR2-S2814A, RyR2-S2814D, and their WT were from the laboratory of Dr. X.H.T. Wehrens (Chelu et al., 2009). Hearts were extracted and hung on a Langendorff apparatus where they were perfused with either a physiological saline solution or with saline plus 300 nm/liter Iso (Cat#BP-1755; Thermo Fisher Scientific) for 2 min. They were then perfused with glutaraldehyde at a concentration of 4% in a 0.1 mmol/liter cacodylate buffer (Cat#12310; Electron Microscopy Sciences), pH 7.4 for 5 min.

The left ventricular apex of each heart was cut into roughly 1 mm × 1 mm cubes using double-edged razor blades. After fixation, dehydration, infiltration, and resin embedding were done as previously described (Asghari et al., 2009). Briefly, 4–5 cubes from each heart were postfixed in 2% OsO_4 in 1 mmol/liter cacodylate buffer, then stained en block in 2% aquatic saturated uranyl acetate, after which it was gradually dehydrated in ethanol and embedded in a mixture of 50% Spurr's (acrylic) and 50% Epon resins. After 48 h in a 60°C oven, samples were sorted and prepared for sectioning. Using a Leica UC7/FC7 microtome and a 35° diamond knife (DiATOME ultra, 2.5 mm), the

embedded blocks were sectioned to about 80 nm thick for 2-D imaging and 200 nm thick for 3-D imaging. The sections were then placed on 2 mm × 1 mm Cu, Formvar coated slot grids (Electron Microscopy Sciences). After contrast staining, the samples were observed using a 200 kV Tecnai G2 TEM with a LaB6 filament (FEI). We examined two hearts for each of the mutant and WT mice: two blocks per heart, four sections per block, and one section per grid. The same blocks were used for 2-D and 3-D EM. The total number of the dyads examined in each condition is indicated in Fig. 2.

Morphological measurements

The Fiji program (Schindelin et al., 2012) was used for morphometric analysis of randomly collected 2-D EM images from all phosphomutant and WT ventricular tissue. We measured the length of the dyad, defined as the region of close apposition between the jSR and surface or t-tubule membranes, in images at 30K magnification or higher (Lavorato et al., 2015). Fig. S1 displays details of how these measurements were performed. Samples were presented randomly to the individual measuring the lengths (S.S.), who was blinded as to their identity. The WT littermates were used as the controls; there was a single WT mouse for both the S2808A and S2030A mutants (WT 2808_2030), and the WT mice for the S2814A and WT S2814D mutants were pooled (WT 2814). All chemicals were purchased from Sigma-Aldrich unless otherwise stated. Additional details on tissue preparation and EM acquisition are provided in Asghari et al. (2014, 2020).

Electron tomography and classifying RyR2 positions

Each grid was examined on a dual-tilt electron microscope, a 200-kV Tecnai G2 (FEI), and relatively flat dyads were selected for imaging. We used Inspect3D to align the two tilt-series and the multiplanar viewer in Amira 6.4 (Thermo Fisher Scientific) to visualize the tetramers, differentiate between tetramers and membrane, and estimate the location and orientation of every tetramer. This process informed the placement of the tetramers relative to each other and the measurement of their nearest-neighbor distances (NND), as discussed in detail elsewhere (Asghari et al., 2014, 2020). We employed no image processing steps other than a contrast stretch.

Fig. 1 A i displays a single plane from the tomogram acquired from an S2814A mouse heart. Each plane is outlined in a different color; XY red, YZ green, and XZ blue. Bisecting the dyad along the XZ plane provided an en face view of the tetramers (Fig. 1 A ii). In most tomograms, a single plane reveals limited information since the surface of the SR is uneven and not all the tetramers are either normal to the plane or visible. Individual XZ planes were therefore viewed individually through the dyad at 0.5 nm increments to best identify a RyR2 channel and then tilted in X and Y to identify its corners. That tetramer's position and orientation were then mapped with a red box (27 nm^2) and the process was repeated for each tetramer. All the boxes were then displayed on a single plane from which the NND measurements were made (Fig. 1 A iii). We selected relatively flat junctions for tomographic analysis to enable a 2-D projection of the 3-D structure with limited distortion (Asghari et al., 2014).

In Fig. 1 A iv, the tetramers were color-coded to indicate their relative positions. A tetramer was in a checkerboard arrangement (aqua) relative to its nearest neighbor if the sides were parallel, separated by <3 nm and overlapped by <18 nm two-thirds of its length. If those criteria were fulfilled but the overlap exceeded 18 nm, the tetramers were classified as side-by-side (orange). In those instances where the tetramers were farther apart than 3 nm, or their sides were not parallel, they were considered isolated (green) (Asghari et al., 2014). Fig. 1 B displays magnified views of tetramers in various configurations.

Placement of the boxes, tetramer classification, and calculating their center-to-center NND used a C++ program, RyRFit, which is freely available (see Data availability). A detailed example of the process has been published (Asghari et al., 2020). Figs. S2, S3, S4, S5, S6, and S7 display images for the WT 2030_2808, WT 2814, S2808A, S2030A, S2814A, and S2814D hearts, with and without 300 nmol/liter Iso, respectively.

Statistical analyses

Dyad lengths are presented as a violin plot. The data were analyzed using hierarchical data analysis (HDA) to isolate the effects of genetic mutations and Iso from variations within a given experimental group, the cells and mice (Sikkel et al., 2017). The HDA also removes the effects of pseudoreplication. None of the data sets were normally distributed and four of them remained non-normal even after log transformation. For this reason, we compared the results of the non-transformed data with the transformed data; the same data sets were significant in both cases, suggesting that the HDA analysis is not sensitive to the shape of the distribution. In both cases, we applied the Holm–Bonferroni correction for multiple data sets (Holm, 1979). This is preferred to the Bonferroni correction which has a greater family-wise failure rate, and is statistically weak and overly conservative (Olejnik et al., 1997). Tables 1 and 2; and Table S1, have five columns; the first two show the comparison, the third shows the probability calculated by Sikkel's R program for the log-transformed data, and the fourth and fifth show the results from the Holm–Bonferoni test. The P values in column 3 were ranked from smallest to largest and a Holm–Bonferroni critical P value, using $\alpha = 0.05$, was calculated from the ranking, column 4. The comparisons showed a significant difference, column 5, if the actual P value was less than the critical P.

The median, first and third quartiles, and minimum and maximum values for the junction lengths for all of the mice are provided in Table S2, as are the means and standard deviations.

The distribution of the tetramer center-to-center NNDs were compared using the non-parametric k-sample Anderson–Darling test (Scholz and Stephens, 1987) with values of $\alpha < 0.05$ considered significant. All of the groups had significant differences within them. The Holm–Bonferroni correction was used for subsequent pair-wise comparisons within each group. We use the cumulative distribution function (CDF) when displaying distributions as this makes differences easier to visualize.

GraphPad Prism was used for the violin plot, histograms, and CDFs using the Okabe-Ito color palette to accommodate the color blind (Katsnelson, 2021).

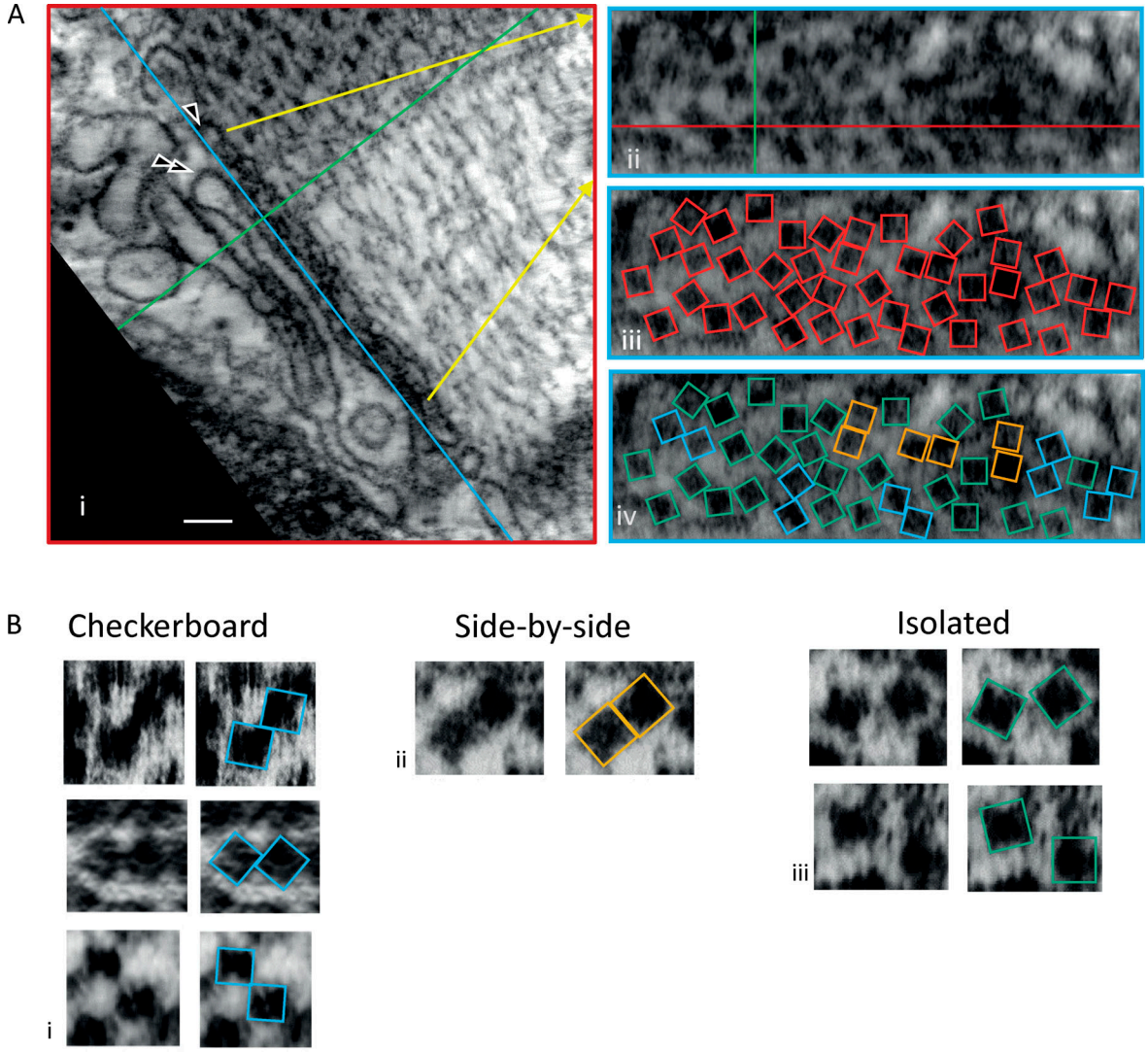

Figure 1. **Tetramer Identification and Classification. (A i)** A single image plane extracted from the dual-tilt tomogram of a mouse (S2814A) left ventricular myocyte fixed in situ. Different orthogonal planes from within the volume of the tomogram are indicated by different colors; XY in red, YZ in green, and XZ in blue. The intersection point of all three planes lies within a single ryanodine receptor and the XZ plane (blue line) was positioned to parallel, as nearly as possible, the jSR (single arrowhead) and t-tubule (double arrowhead) membranes, but to be within the cleft and to bisect the ryanodine receptors. Scale bar is 100 nm. **(A ii)** An en-face view (XZ plane) of the indicated section (yellow arrows, A i) of this junction. **(A iii)** The position of the tetramers has been identified by red boxes 27 × 27 nm. **(A iv)** Tetramers were color-coded to indicate their orientation relative to their nearest-neighbor; checkerboard—aqua, side by side—orange, isolated—green. **(B)** Examples of the different tetramer–tetramer contacts.

Online supplemental material

Fig. S1 is a 2-D electron micrograph acquired from a WT 2030_2808 mouse. The images demonstrate how the lengths of the dyads were measured. Fig. S2 shows a single plane from the tomogram of a WT 2030_2808 mouse treated with either saline (A i) or Iso (B i). The corresponding images, A ii and B ii, show the position of all of the tetramers identified in that dyad as well as their center-to-center NNDs. Figs. S3, S4, S5, S6, and S7 are comparable images for WT 2814, S2808A, S2030A, S2814A, and S2814D mice, respectively. Table S1 shows hierarchical data analysis (HDA). Table S2 lists the median, first and third quartiles, and minimum and maximum values for the junction lengths for all of the mice.

Results

Dyad lengths

Superresolution immunofluorescence imaging indicated that RyR2 cluster sizes are significantly increased by a phosphorylation cocktail (Asghari et al., 2020), suggesting that physiological stimuli might also regulate the size of the dyads. To test that hypothesis, we measured the 2-D length of mouse dyads in transmission electron micrographs. Fig. 2 A shows examples of dyadic clefts that had been perfused with saline or with saline plus 300 nmol/liter Iso; arrows show the endpoints of the measurements. The data is displayed in violin plots, Fig. 2 B; the median, first, and third quartiles are indicated with horizontal lines.

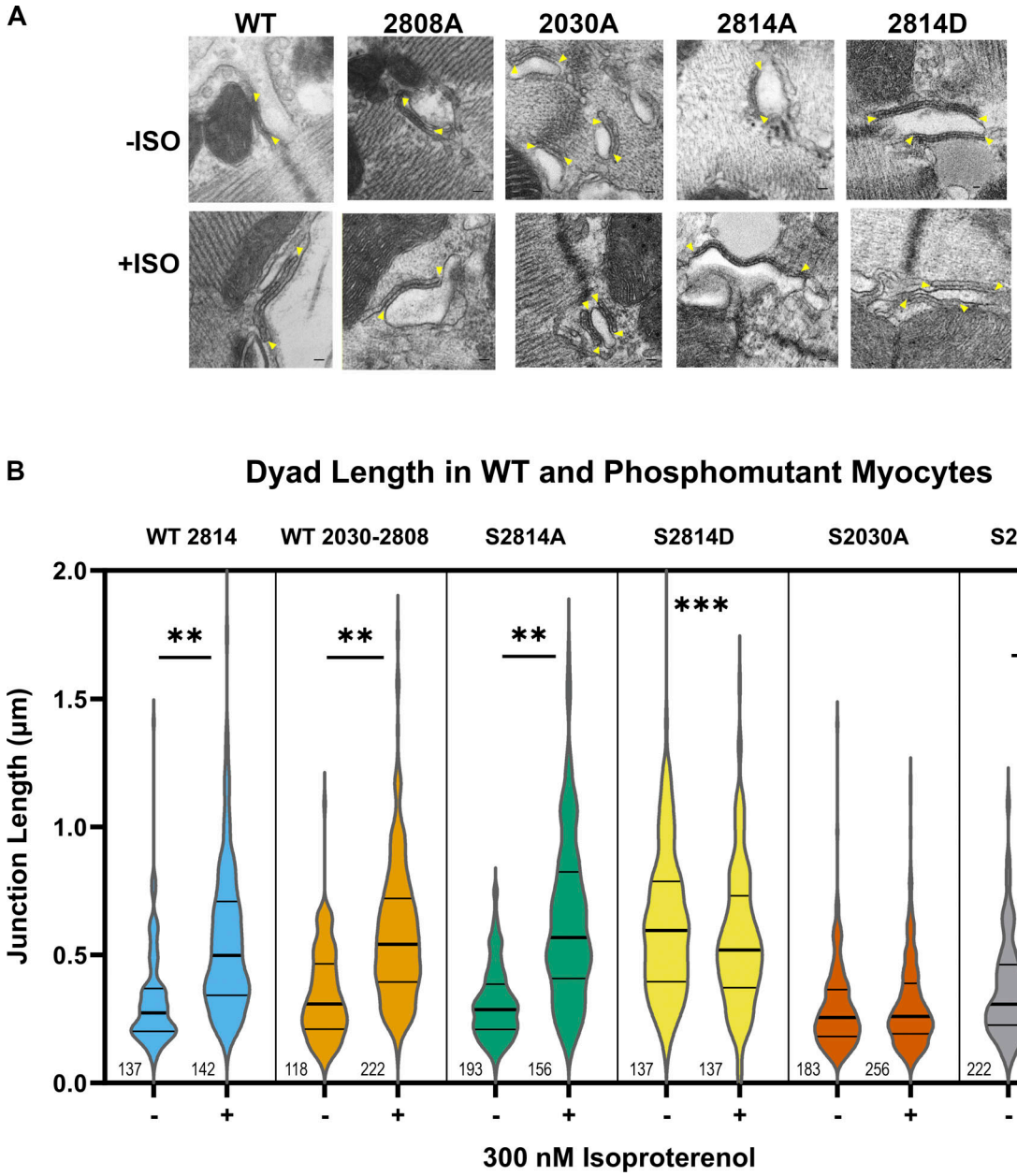

Figure 2. **Dyad lengths. (A)** TEM images under the indicated conditions, arrows indicate dyads' extent. Scale bar = 50 nm. **(B)** Violin plots of the dyad lengths. ** indicates a significant difference between the given mutant and its ISO-treated counterpart ($P < 0.01$). In the non-ISO-treated hearts, dyads in the S2814D mouse were significantly longer than all others (***, $P < 0.001$).

For clarity, the results of the hierarchical analysis are presented in their entirety in Table S1. Selected comparisons are in Tables 1 and 2.

Table 1 shows the comparison between the dyad lengths of the saline-treated mouse hearts and their Iso-treated counterpart. Both WT mice showed highly significant increases in dyad length in response to Iso, as did the S2808A and S2814A myocytes. Notably, no changes were seen in either the S2814D or the S2030A mutants.

The effects of the S2814D mutation are highlighted in Table 2. At rest, its dyad was significantly longer than the others, and with the exception of S2030A, it was no different from those that had been treated with Iso. Perfusing the S2814D hearts with Iso had no further effect on the length of their dyads.

Measuring the length of the dyad, following the curve of the membrane, is a simple measurement, but it produces clear results. The dyad cross-sections are a 2-D view of a 3-D volume that extends in both directions in the Z dimension. We do not know where our cross sections lie relative to the dyad's maximum diameter, nor how they are oriented with respect to it. Thus, the measured cross-sections represent cuts at random positions and angles through the junction. For these cuts to produce a significant change in length, it is highly likely there was an expansion of the dyad's area, not just its length.

Table 1. **Effect of ISO on dyad length in WT and phosphomutant mouse ventricle**

			Holm–Bonferroni	
Comparison		HDA P value	Critical P value	Significant
WT_2814	WT_2814_Iso	9.88E-07	1.25E-03	YES
S2814A	S2814A_Iso	2.45E-08	9.43E-04	YES
S2814D	S2814D_Iso	8.82E-02	1.85E-03	
WT 2030_2808	WT 2030_2808_Iso	2.86E-07	1.14E-03	YES
S2030A	S2030A_Iso	7.87E-01	1.00E-02	
S2808A	S2808A_Iso	7.21E-07	1.19E-03	YES

Table 2. **S2814D: Pairwise comparison of dyad lengths**

			Holm–Bonferroni	
Comparison		HDA P value	Critical P value	Significant
S2814D	WT 2814	9.05E-09	8.77E-04	YES
S2814D	WT 2030_2808	9.53E-08	1.04E-03	YES
S2814D	S2808A	8.09E-07	1.22E-03	YES
S2814D	S2814A	1.18E-08	8.93E-04	YES
S2814D	S2030A	4.06E-10	7.58E-04	YES
S2814D	WT_2814_Iso	1.85E-01	2.50E-03	
S2814D	WT 2030_2808_Iso	5.99E-01	5.56E-03	
S2814D	S2808A_Iso	9.89E-01	5.00E-02	
S2814D	S2814A_Iso	9.70E-01	2.50E-02	
S2814D	S2030A_Iso	1.91E-09	8.06E-04	YES
S2814D_Iso	WT 2030_2808_Iso	1.91E-01	2.63E-03	
S2814D_Iso	WT_2814_Iso	6.87E-01	8.33E-03	
S2814D_Iso	S2808A_Iso	7.64E-02	1.79E-03	
S2814D_Iso	S2814A_Iso	9.64E-02	1.92E-03	
S2814D_Iso	S2030A_Iso	6.62E-07	1.16E-03	YES

Tetramer orientations and NNDs

Wild types

Fig. 3, A i and B i, display the RyR2 NND and orientation histograms obtained from the WT 2030_2808 and WT 2814 mice; an example of the tomograms and tetramer placements for saline and Iso perfused hearts are in Figs. S2 and S3. The histograms were bimodal, with one mode (~28 nm) dominated by tetramers in the side-by-side (orange) orientation and the second (~34 nm) by those in a checkerboard (aqua). A few tetramers were classified as isolated (green). The percentage of tetramers in each orientation and the number of tomograms and tetramers examined are listed in Table 3.

Perfusing the WT mouse hearts with Iso for 2 min resulted in unimodal histograms with peaks at ~34 nm (Fig. 3, A ii and B ii). These changes were accompanied by a large increase in the proportion of tetramers in the checkerboard orientation and a correspondingly large decrease in those that were side by side, while those in the isolated configuration remained few in number (Table 3).

Both WT responded to Iso with an increase in their tetramer NNDs, which is reflected in a significant rightward shift of their CDFs. The saline-perfused WTs were not significantly different from each other, neither were their Iso-treated counterparts, Fig. 3 C and Table 4. The histograms and tetramer orientations of the saline-perfused WT mice were similar to those recorded from rats and humans (Asghari et al., 2014, 2020), resulting in comparable CDFs, Fig. 3 D.

Phosphomutants

Figs. 4 A (S2808A), 4 B (S2030A), 5 A (S2814A), and 5 B (S2814D) display NND histograms from myocytes whose hearts had been perfused with saline (i) or saline plus Iso (ii), and the corresponding CDFs (iii). The tetramer orientations and the number of tetramers and tomograms examined are in Table 3. Images of the tomograms and tetramer placements for the saline and Iso-perfused hearts are in Figs. S4 (S2808A), S5 (S2030A), S6 (S2814A), and S7 (S2814D).

S2808A

The NND distribution (Fig. 4 A i), tetramer orientations (Table 3), and the CDF (Fig. 4 A iii and Table 4) were identical to that of the WT.

On application of Iso, the CDFs were not significantly different but the orientations showed a significant difference in their response. Treatment with Iso caused a large reduction in the proportion of isolated tetramers in the WT from 15.0% to 6.7%. Iso had the opposite effect in this mutant, with the proportion of isolated tetramers increasing from 16.7% to 23.9%, with an associated drop in the checkerboard from 81.3% to 63.8%.

S2030A

This NND distribution was bimodal (Fig. 4 B i) comparable with WT, and the CDFs were not significantly different (Table 4). Despite this the tetramer orientations were very different, with double the proportion of isolated, and roughly an equal distribution between checkerboard, side-by-side and isolated (Table 3).

The Iso response showed a significant change in the CDF (Table 4) compared with the WT although the tetramers with an NND < 32 nm seemed to have a muted response, probably because the proportion of side-by-side tetramers was largely unchanged. There was only a small increase in the checkerboard and a comparable decrease in the isolated.

S2814A

Although the NND distribution of this mutant was bimodal (Fig. 5 A i), the modes corresponded to unusual orientations, with one at 31 nm composed largely of checkerboard and the second at 35 nm with roughly equal proportions of checkerboard and isolated. The number of isolated tetramers was three times that of the WT (37.6% versus 13.0%), the side-by-side was halved (17.4% versus 33.1%), and there were fewer checkerboards (45.0% versus 53.9%). The result of these changes was a highly disorganized array (Fig. 1 A).

The NND distribution of the Iso-treated myocytes appeared not as broad and was unimodal with a peak between 32 and 34

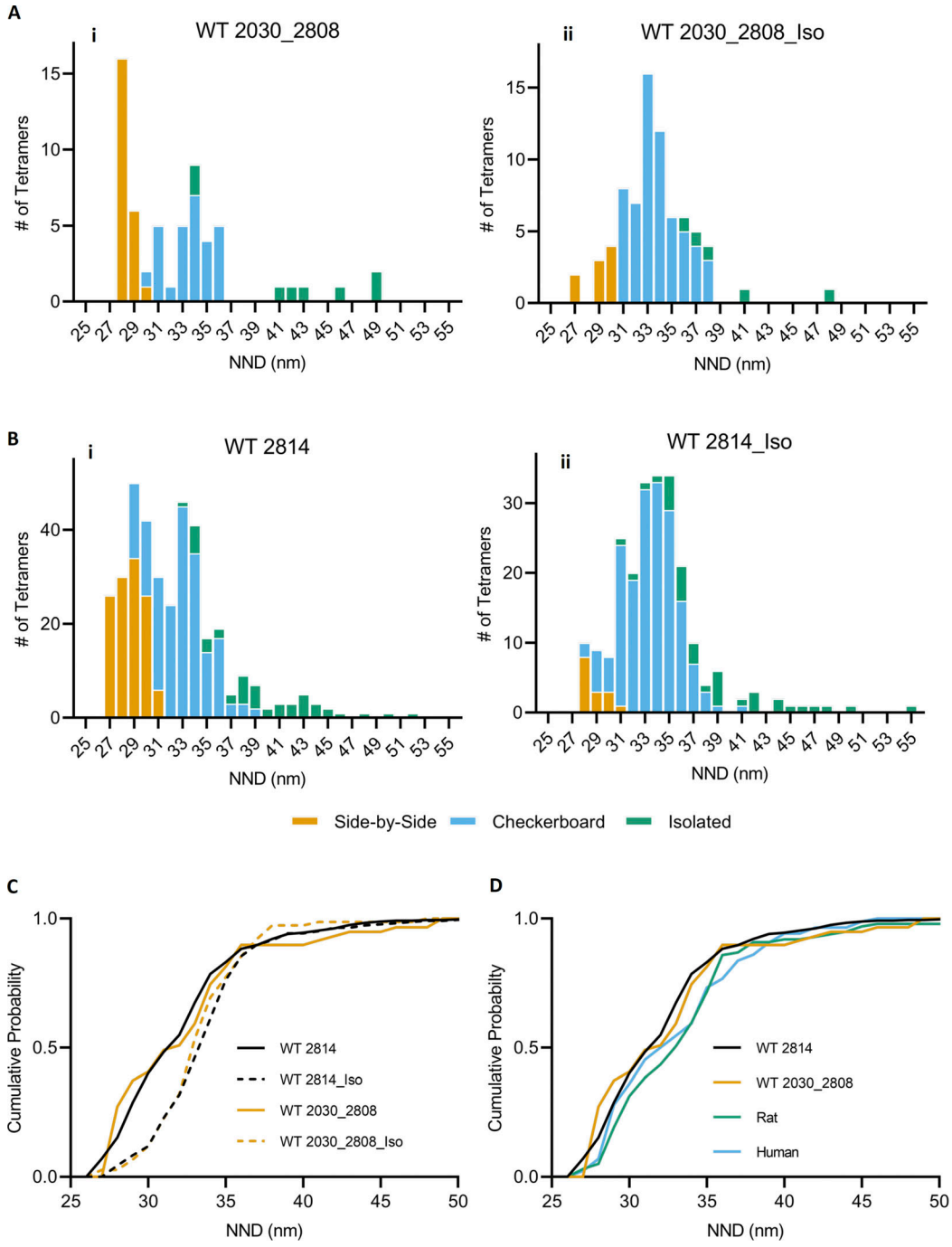

Figure 3. **NND and CDF of WT mice with and without Iso; CDF of rat, human, and WT mice. (A and B)** NNDs of RyR2 were acquired from WT S2030_S2808 (A) and WT 2814 (B) mice, (i) at rest and (ii) from mice whose hearts had been treated with ISO. **(C)** CDF of tetramer NND acquired from WT mice hearts perfused with saline and from those treated with ISO. **(D)** CDF of tetramer NND comparing WT mice with rats and humans.

nm, smaller than the WT (Fig. 5 A ii). This change reflected a 60% drop in the isolated tetramers, to 14.4%, particularly those at NND > 40 nm, and a corresponding rise in the checkerboard (69.8%), while the side-by-side was unchanged (Table 3).

The rightward shift of the CDF in response to Iso seen in WT mice and rats reflects a movement of side-by-side tetramers to a largely checkerboard configuration. In this case, the proportion of side-by-side tetramers in the S2814A mice was low and changed minimally in response to ISO, so that part of the CDF was already shifted and there was no further change. The result was that the S2814A CDF was significantly different from the WT 2814 but not from the S2814A_Iso (Table 4).

S2814D

The NND distribution had a single peak at ~33 nm reflecting the small proportion of tetramers in the side-by-side orientation, with a large increase in the number of isolated and a small increase of the checkerboard (Fig. 5 B i and Table 3). The sharp

Table 3. **Tetramer orientations (%)**

Mouse	Checkerboard	Side-by-side	Isolated	# of tomograms	# of tetramers	# of mice
WT S2030-S2808	46.7	38.3	15.0	3	60	2
WT S2030-S2808 + Iso	81.3	12.0	6.7	3	75	2
S2808A	39.3	44.0	16.7	4	84	2
S2808A + Iso	63.8	12.3	23.9	7	138	2
S2030A	35.0	32.0	33.0	6	103	2
S2030A + Iso	44.7	29.8	25.4	6	114	2
WT S2814	53.9	33.1	13.0	17	369	2
WT S2814 + Iso	76.3	7.9	15.8	13	227	2
S2814A	45.0	17.4	37.6	4	109	2
S2814A + Iso	69.8	14.4	15.8	9	139	2
S2814D	60.7	11.9	27.4	6	135	2
S2814D + Iso	78.6	7.1	14.3	6	84	2

reduction in the side-by-side is similar to Iso-perfused WT hearts and in rats after exposure to a phosphorylation cocktail (Asghari et al., 2014, 2020), and is consistent with S2814D being a phosphomimetic. As a result, the CDF was shifted to the right and was not significantly different from the WT treated with Iso (Table 4).

Iso produced little change in the NND distribution, Fig. 5 B ii, resulting in no significant difference between the CDFs of S2814D and S2814D_Iso or between S2814D_Iso and WT 2814_Iso. There was a very large increase in the number of tetramers in the checkerboard orientation, a large decrease in the isolated and a minimal change in the side-by-side (Table 3).

Discussion

Dyad lengths

We have found that the size of the dyad in WT and mutant mouse ventricular myocytes, with the notable exceptions of S2814D and S2030A, was significantly increased by a 2-min exposure to 300 nmol/liter Iso.

The lengths of the dyads in the saline-perfused S2814D hearts were equivalent to those of WT + Iso. That the expansion of the dyad is produced by a single mutation in RyR2 implies a direct link between the state of the tetramer and the architecture of the membrane in which it is embedded. The lack of further response of the S2814D + Iso cells suggests that the effect of phosphorylation of other sites on RyR2 is not additive and that the expansion derived from S2814D alone is near maximal.

In considering whether the changes in dyad length that we attribute to the mutations alone could be due to changes in the expression of RyR2 or its associated proteins, we note that within the limits of detection of the Western blotting technique, there were no changes in the expression of RyR2, $Ca_v1.2$, or the Na^+/Ca^{2+} exchanger in the S2814D mice (van Oort et al., 2010). If there had been undetectable changes in expression, this would not explain the lack of response to Iso. The expansion of the dyads of WTs, S2080A, and S2814A in response to Iso is too rapid to be explained by changes in protein expression. This data taken together with the S2814D behavior suggests a connection between the RyR2 and the jSR, which quickly affects the size of the dyad.

We do not know what the link might be and whether it is direct or via RyR2's attendant proteins, although there is evidence that the phosphomimetic S2814D has a changed RyR2 proteome (Chiang et al., 2021). Notably, the application of Iso produced no expansion of the dyad in the S2030A mouse. Whether the lack of response is due to interrupting this link or through another mechanism is unknown.

Direct, real time, visualization of the SR and t-tubule in living murine myocytes has demonstrated that dyads are highly mobile structures that are continuously and rapidly changing in number, shape, size, and position (Vega et al., 2011; Drum et al., 2020). Within minutes, dyads were seen to form, disappear, and split into smaller pieces; a movement driven in part by the microtubule motor proteins kinesin-1 and dynein, both of which are subject to regulation by a host of posttranslational modifications that alter the direction of movement, the transit time, and the binding and unbinding of their cargo (Barlan and Gelfand, 2017; Kumari and Ray, 2022). In this paradigm, the size of the dyads we observed in our fixed tissues were snapshots of this dynamic process. Iso, which activates PKA and, through Epac 2, CamKII (Pereira et al., 2013), could shift the equilibrium to one in which larger more stable dyads are favored. Recent research has also demonstrated that motor-cargo adaptors, including integral membrane proteins, can recruit kinesin and dynein to an organelle to regulate its transport (Cross and Dodding, 2019). Our results with the S2814D and S2030A mice suggest that the phosphorylation status of RyR2 is a central element in these processes either directly or indirectly through its binding partners (Chiang et al., 2021).

The nanoscopic domain formed by the dyad is a critical determinant of excitation–contraction coupling (ECC). Within its femtoliter volume, diffusion is restricted to enable the ion channels, signaling molecules, and regulatory proteins on the opposing membranes to control SR Ca^{2+} release independently of reactions within the bulk myoplasm. Changing its size, as we have observed, would be expected to change the number and

Table 4. **CDF comparisons**

Group	Paired comparison		P	Critical P value	Significant
WT mice	WT 2814	WT 2814_Iso	1.5E-12	8.0E-03	YES
	WT 2814	WT 2030_2808_Iso	2.8E-05	1.0E-02	YES
	WT 2814_Iso	WT 2030_2808	8.1E-05	1.3E-02	YES
	WT 2030_2808	WT 2030_2808_Iso	1.7E-03	1.7E-02	YES
	WT 2814	WT 2030_2808	2.1E-01	2.5E-02	
	WT 2814_Iso	WT 2030_2808_Iso	5.5E-01	5.0E-02	
Species	WT 2814	Rat	3.4E-03	8.0E-03	YES
	WT 2814	Human	1.3E-02	1.0E-02	
	WT 2030_2808	Rat	3.6E-02	1.3E-02	
	WT 2030_2808	Human	4.4E-02	1.7E-02	
	WT 2814	WT 2030_2808	2.1E-01	2.5E-02	
	Rat	Human	5.7E-01	5.0E-02	
S2808A	WT 2030_2808	S2808A_Iso	1.6E-03	8.0E-03	YES
	S2808A	S2808A_Iso	1.7E-03	1.0E-02	YES
	WT 2030_2808	WT 2030_2808_Iso	1.7E-03	1.3E-02	YES
	WT 2030_2808_Iso	S2808A	2.2E-03	1.7E-02	YES
	WT 2030_2808_Iso	S2808A_Iso	4.6E-02	2.5E-02	
	WT 2030_2808	S2808A	2.2E-01	5.0E-02	
S2030A	WT 2030_2808	WT 2030_2808_Iso	1.7E-03	8.0E-03	YES
	WT 2030_2808	S2030A_Iso	2.3E-03	1.0E-02	YES
	S2030A	S2030A_Iso	2.9E-03	1.3E-02	YES
	WT 2030_2808_Iso	S2030A	5.7E-03	1.7E-02	YES
	WT 2030_2808_Iso	S2030A_Iso	3.1E-02	2.5E-02	
	WT 2030_2808	S2030A	5.3E-01	5.0E-02	
S2814A	WT 2814	S2814A	4.8E-13	8.0E-03	YES
	WT 2814	WT 2814_Iso	1.5E-12	1.0E-02	YES
	WT 2814	S2814A_Iso	7.0E-09	1.3E-02	YES
	WT 2814_Iso	S2814A	4.5E-03	1.7E-02	YES
	S2814A	S2814A_Iso	2.7E-02	2.5E-02	
	WT 2814_Iso	S2814A_Iso	2.9E-01	5.0E-02	
	WT 2814	WT 2814_Iso	1.5E-12	8.0E-03	YES
	WT 2814	S2814D	1.2E-04	1.0E-02	YES
	WT 2814	S2814D_Iso	1.7E-04	1.3E-02	YES
	WT 2814_Iso	S2814D	3.3E-02	1.7E-02	
	WT 2814_Iso	S2814D_Iso	8.8E-02	2.5E-02	
	S2814D	S2814D_Iso	7.0E-01	5.0E-02	

spatial distribution of the molecules therein, which would impact Ca^{2+} dynamics, the probability of Ca^{2+} spark formation (Iaparov et al., 2021), and the efficacy of ECC.

Organization of the tetramer array

WT mice

Under basal conditions, the tetramers in the WT mouse ventricular dyads were distributed similarly to each other and to rats and humans, with a bimodal CDF of their NND reflecting a mixture of checkerboard and side-by-side orientations. Most of the tetramers were in contact with one or more neighbors, though a few were isolated (Fig. 3 D).

Cabra et al. (2016) have observed tetramer–tetramer interactions using cryo-electron microscopy to examine purified RyR2 laid on a carbon-coated grid. Despite the near-infinite number of possible interactions between tetramers under

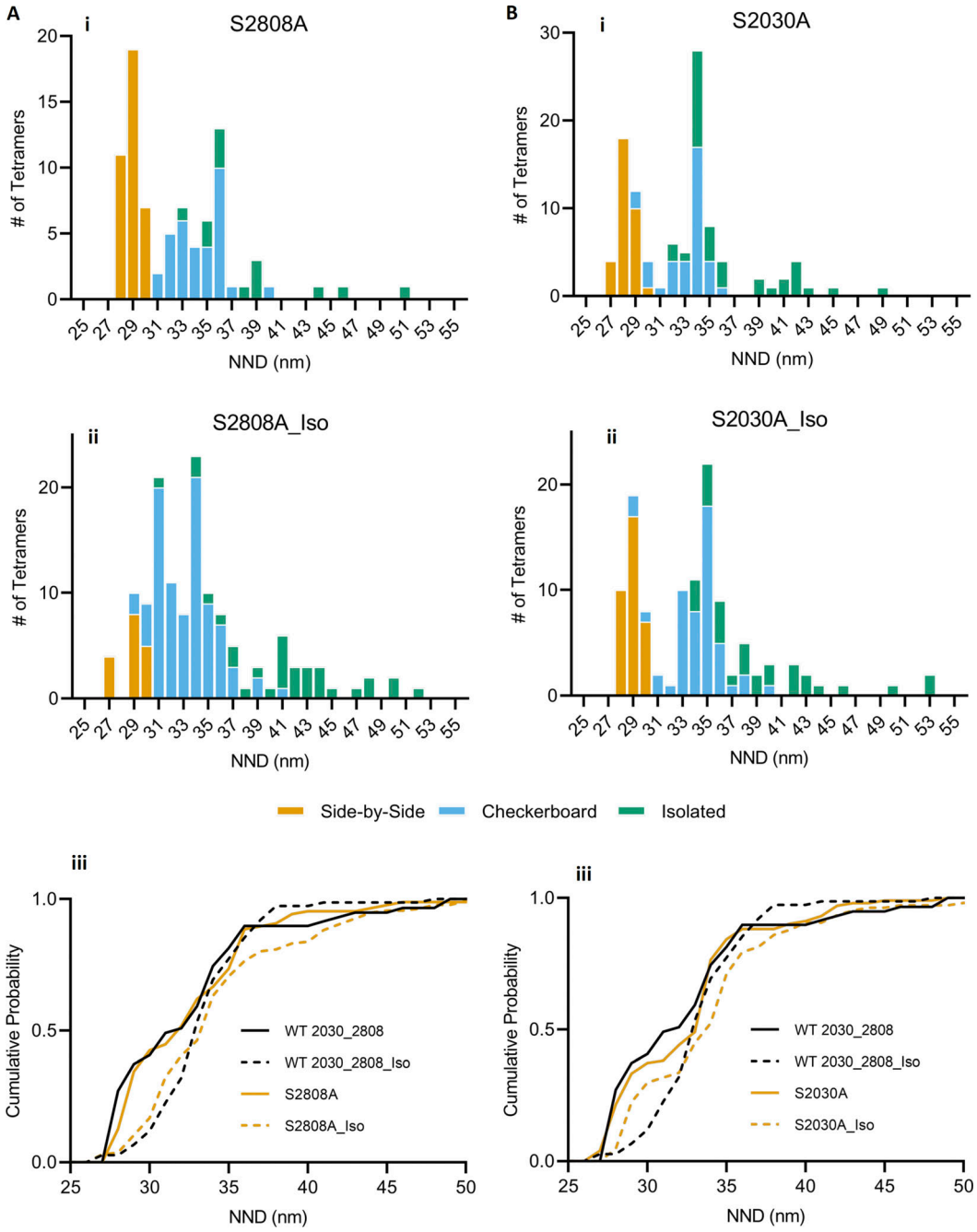

Figure 4. **S2808A and S2030A; NND and CDF with and without Iso. (A and B)** NNDs of RyR2 were acquired from S2808A (A) and S2030A (B) mice hearts, (i) saline-perfused and (ii) treated with ISO. CDF of tetramer NND acquired from (A iii) S2808A and (B iii) S2030A hearts perfused with saline or Iso compared to their WT.

these experimental conditions, they saw only a few, distinct, configurations termed adjoining and oblique, which correspond well to our side-by-side and checkerboard, respectively. The proportion in each configuration could be adjusted by changing the Ca^{2+} concentration, indicating that the interactions may be sensitive to physiologically relevant parameters.

That similar tetramer–tetramer contacts have been visualized in vivo in three different species and in vitro using vastly different techniques suggests that intertetramer interaction is real and an integral part of the array's normal structure and function. This conclusion is further supported by our observations using dSTORM immunofluorescence microscopy, which also demonstrates tetramer–tetramer contacts similar to those we have described (Scriven et al., 2023).

Treatment with Iso resulted in fewer side-by-side tetramers and an increase in the checkerboard (Fig. 2, A ii and B ii; and Table 3), which was reflected by a rightward shift of the CDF (Fig. 2 C). We observed the same changes in tetramer orientation and NND CDF from rat myocytes that were enzymatically dissociated, permeabilized, and treated with a phosphorylation

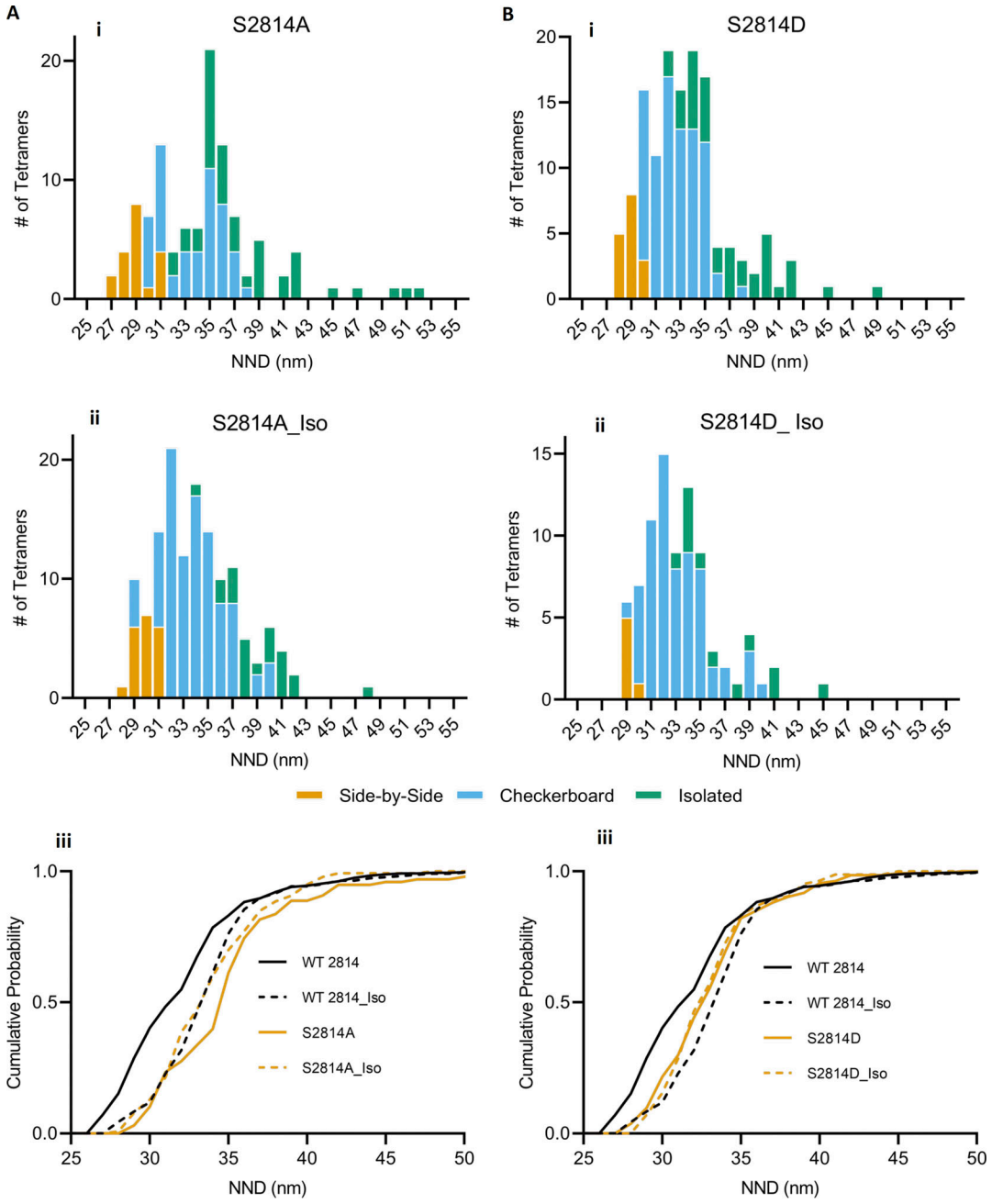

Figure 5. **S2814A and S2814D; NND and CDF with and without Iso. (A and B)** NNDs of RyR2 were acquired from S2814A (A) and S2814D (B) mice hearts, (i) saline-perfused and (ii) treated with ISO. CDF of tetramer NND acquired from (A iii) S2814A and (B iii) S2814D hearts perfused with saline or Iso compared to their WT.

cocktail that activated numerous kinases and inhibited the major phosphatases (Asghari et al., 2014, 2020). Taken together, these results show that activation of the β-adrenergic receptor induces tetramer reorganization as well as expansion of the dyad, indicating that both are part of the normal fight-or-flight response.

In all of our experiments, changes in the CDF and tetramer orientation were accompanied by a change in the length of the dyad, with the exception of S2030A. In this mutant, some of the side-by-side and isolated tetramers reoriented into a checkerboard configuration resulting in a significant shift of the CDF, but the length of the dyad was unchanged. This implies that changes in the size of the dyad and the tetramers' relative positions and orientations are the result of different processes.

Phosphomutant mice

All of the substitutions produced significant changes in the organization of the array compared with their WT counterparts. In particular, they had an abnormally large number of isolated tetramers either after treatment with Iso (S2808A), before Iso (S2814A, S2814D), or both before and after (S2030A), indicating that all of these residues are involved in the normal structure of

the array and in its restructuring in response to β-adrenergic stimulation. How the mutations affect the tetramer–tetramer contacts or the long-range allosteric interactions required to open the channel (Peng et al., 2016) is unknown.

The majority of the RyR2 in the S2814D mutant were in a checkerboard configuration, which combined with the low number of side-by-side, and the rightward shift in the CDF, was close to the expected configuration of the array after treatment with Iso (Fig. 5 B and Table 3). This suggests that phosphorylation of the tetramer itself affects both the size of the dyad and the organization of the array but does not preclude these events being mediated by different processes as suggested by the results from the 2030A mouse. Treating this mouse with Iso produced a further shift in the tetramers' organization, becoming indistinguishable from WT + Iso, indicating that phosphorylation of other residues or downstream targets is required to complete the transition.

The position of the CDF in the S2814A mouse was comparable with WT + Iso and typical of an array with a much higher proportion of tetramers in the checkerboard configuration (Fig. 5 A and Table 3). In this case, it was due to a large number of isolated tetramers that were located at a sufficient distance from each other to shift the CDF to a significantly longer NND. The result was a highly disordered array (Fig. 1). Like S2814D, treating this mutant with Iso resulted in an array that closely resembled WT + Iso.

We conclude that although phosphorylation of S2814 alone mimics β-adrenergic stimulation, the S2814A results suggest this residue is not necessary to elicit a response. The limited movement of the CDF and change in tetramer reorientation in response to Iso in the S2030A mutant, and the abnormal proportion of isolated tetramers following Iso in the S2808A suggest that both of these residues are needed.

Structure and function

The conclusions derived from the structural analyses that S2808 and S2030 are necessary for normal β-adrenergic response, while S2814 is not, concurs with results from functional studies that have used the same transgenic mouse models. Briefly, these analyses have demonstrated that with matched Ca^{2+} current, Ca^{2+} transient, and SR Ca^{2+} load, Iso produces less SR Ca^{2+} release from S2030A myocytes than from WT, resulting in a significantly lower ECC gain (Potenza et al., 2019). In the S2808A mutant, Iso results in a loss of intraluminal Ca^{2+} sensitivity and spatiotemporal synchronization of RyR2 release relative to WT (Ullrich et al., 2012; Potenza et al., 2020) but without affecting ECC gain (Benkusky et al., 2007; Ullrich et al., 2012). Both of these residues are therefore necessary for a normal β-adrenergic response. Conversely, S2814A mice appear to have normal ECC parameters in response to Iso (Grimm et al., 2015; Baier et al., 2021), so phosphorylation of this residue is not required.

Our structural analysis of the S2814D dyads suggested that the pseudophosphorylation was a gain-of-function mutation, a condition that has been observed (van Oort et al., 2010). They reported that this mutant has a high Ca^{2+} spark rate despite a significantly reduced SR Ca^{2+} load. This change is proarrhythmogenic and has been linked to elevated diastolic Ca^{2+} leak in both patients and animals with heart failure (Ai et al., 2005; Ling et al., 2009), suggesting prolonged phosphorylation of this residue is pathological (Grimm et al., 2015).

The presumptive mechanism linking RyR2 phosphorylation to cardiac function is changes in single-channel gating. Such effects have been recorded from isolated channels in artificial bilayers, but the magnitude of the changes in open probability do not match those seen in vivo (Benkusky et al., 2007; Xiao et al., 2007; van Oort et al., 2010; Potenza et al., 2019). This difference may be explained, in part, by the direct link we have identified between the state of the tetramer and the jSR, which is absent with purified RyR2 and unlikely to be preserved by heavy SR vesicles painted onto an artificial bilayer. Tetramer–tetramer contacts, also routine in vivo, are seldom observed in vitro and are important as our conceptual model postulates that intertetramer contacts modify channel gating, which has been observed with both RyR2 (Marx et al., 2001) and RyR1 (Porta et al., 2012).

We have compared the changes in the Ca^{2+} spark rate of the mutants relative to WT, both with and without Iso (or CaMKII in the case of S2814D), with our model's predictions (Table 5). All of our predictions are in agreement with experimental observations, with the exception of S2814A. Given the low proportion of side-by-side tetramers both at rest and after Iso, we predicted a high Ca^{2+} spark rate under both conditions, which was not observed. At rest, the spark rate is comparable with WT (Uchinoumi et al., 2016) but after Iso, the SR Ca^{2+} leak rate/Ca^{2+} load ratio (a combination of Ca^{2+} spark and non-spark diastolic release), while significantly elevated in WT, is unchanged or even slightly lower in this mutant (Baier et al., 2021).

Despite the fact that our original model did not take into account the isolated tetramers, which are present in large numbers in the mutants, our model is successful in predicting the behavior of WT rats and mice, and the majority of the mutants (Table 5). The sole exception, S2814A, cannot be explained with our model unless we assume that this mutation interrupts positive allosteric interaction associated with the checkerboard configuration in some way. This could prevent the increase in spark frequency predicted by the model and align it with the experimental data but lacks evidence and remains a speculation.

In conclusion, we have found that both the size of the dyad and the arrangement of the tetramers are dynamically altered by the application of the β-adrenergic receptor agonist, Iso. The changes induced by the phosphomutant S2814D implied a link between the state of the tetramer, the size of the dyad, and the tetramer organization.

In agreement with functional data, we found that S2808 and S2030 are necessary for the β-adrenergic response, while S2814 may not be. The disposition of the tetramers and the correlation of structure with function both at rest and in response to Iso suggests that tetramer–tetramer contacts play an important functional role. We have proposed that the contacts modify the tetramers' gating parameters, possibly by changing allosteric interactions.

In this paper and its companion (Scriven et al., 2023), we have observed comparable tetramer distributions, both on the surface and in the interior, despite different methodologies and

Table 5. **Change in CaSpF in phosphomutant myocyte compared to WT: Model prediction versus experimental observation**

	Control		Phosphorylated	
	Model	Observed	Model	Observed
S2030A (Potenza et al., 2019)	↓	↓	↓	↓
S2808A (Potenza et al., 2020)	↔	↔	↑	↑
S2814D (van Oort et al., 2010; Uchinoumi et al., 2016)	↑	↑	↔	↔
S2814A (Baier et al., 2021)	↑	↔	↑	↔

The relative change in Ca^{2+} spark frequency of the indicated phosphomutant myocyte relative to its WT is indicated by an arrow. The columns compare the change predicted by the model to the observed result for myocytes at rest (Control) and after phosphorylation by treatment with either Iso (S2030A, S2808A, and S2814A) or CaMKII (2814D).

fixation protocols. Both indicate the tetramers are in an irregular, but non-random, distribution with numerous tetramer–tetramer contacts. We found, separately, that Iso produces significant and rapid changes in the structure. While our results are snapshots of the state of the dyad before and after the application of an agonist, the implication is that the structure is continuously shifting in response to changes in the local environment.

Data availability

The data underlying all the figures and tables in the manuscript are openly available at Zenodo: https://doi.org/10.5281/zenodo.10408329. The full code for the tetramer fitting program, RyRFit is openly available at Zenodo: https://doi.org/10.5281/zenodo.10436621. This program can be compiled to run in either Windows or Linux. A Windows-compatible installation file RyRFit_Installer.exe is also available from GitHub at https://github.com/DScriven/RyRFit, and can be used to install the program which can then read, display, and analyze the image data sets.

Acknowledgments

David A. Eisner served as editor.

E.D.W. Moore acknowledges a grant from the Canadian Institutes of Health Research (148527). H.H. Valdivia is funded by a grant from the US National Institutes of Health (NIH) (R01-HL055438). X.H.T. Wehrens is funded by grants from the US NIH (HL089698, HL147108, HL153350). We used the University of British Columbia's BioImaging Facility's resources (RRID: SCR_021304).

Author contributions: P. Asghari: Conceptualization, Resources, Investigation, Formal Analysis, Data Curation, Visualization, Writing—Original Draft, and Writing—Review & Editing, D.R.L. Scriven: Software, Formal Analysis, Visualization, Writing—Original Draft, and Writing—Review & Editing. S. Shahrasebi: Investigation. H.H. Valdivia: Resources, and Writing—Review & Editing. K.M. Alsina: Resources. C.R. Valdivia: Resources. J.A. Navarro-Garcia: Resources. X.H.T. Wehrens: Resources, Writing—Review & Editing. E.D.W. Moore: Conceptualization, Formal Analysis, Visualization, Writing—Original Draft, Writing—Review & Editing, Funding Acquisition, and Supervision.

Disclosures: The authors declare no competing interests exist.

Submitted: 28 January 2022
Revised: 23 January 2023
Revised: 28 December 2023
Accepted: 31 January 2024

References

Ai, X., J.W. Curran, T.R. Shannon, D.M. Bers, and S.M. Pogwizd. 2005. Ca^{2+}/calmodulin-dependent protein kinase modulates cardiac ryanodine receptor phosphorylation and sarcoplasmic reticulum Ca^{2+} leak in heart failure. *Circ. Res.* 97:1314–1322. https://doi.org/10.1161/01.RES.0000194329.41863.89

Asghari, P., M. Schulson, D.R. Scriven, G. Martens, and E.D. Moore. 2009. Axial tubules of rat ventricular myocytes form multiple junctions with the sarcoplasmic reticulum. *Biophys. J.* 96:4651–4660. https://doi.org/10.1016/j.bpj.2009.02.058

Asghari, P., D.R. Scriven, M. Ng, P. Panwar, K.C. Chou, F. van Petegem, and E.D. Moore. 2020. Cardiac ryanodine receptor distribution is dynamic and changed by auxiliary proteins and post-translational modification. *Elife.* 9:e51602. https://doi.org/10.7554/eLife.51602

Asghari, P., D.R. Scriven, S. Sanatani, S.K. Gandhi, A.I. Campbell, and E.D. Moore. 2014. Nonuniform and variable arrangements of ryanodine receptors within mammalian ventricular couplons. *Circ. Res.* 115:252–262. https://doi.org/10.1161/CIRCRESAHA.115.303897

Baddeley, D., I. Jayasinghe, L. Lam, S. Rossberger, M.B. Cannell, and C. Soeller. 2009. Optical single-channel resolution imaging of the ryanodine receptor distribution in rat cardiac myocytes. *Proc. Natl. Acad. Sci. USA.* 106:22275–22280. https://doi.org/10.1073/pnas.0908971106

Baier, M.J., J. Noack, M.T. Seitz, L.S. Maier, and S. Neef. 2021. Phosphorylation of RyR2 Ser-2814 by CaMKII mediates β1-adrenergic stress induced Ca^{2+} -leak from the sarcoplasmic reticulum. *FEBS Open Bio.* 11:2756–2762. https://doi.org/10.1002/2211-5463.13274

Barlan, K., and V.I. Gelfand. 2017. Microtubule-based transport and the distribution, tethering, and organization of organelles. *Cold Spring Harb. Perspect. Biol.* 9:a025817. https://doi.org/10.1101/cshperspect.a025817

Benkusky, N.A., C.S. Weber, J.A. Scherman, E.F. Farrell, T.A. Hacker, M.C. John, P.A. Powers, and H.H. Valdivia. 2007. Intact beta-adrenergic response and unmodified progression toward heart failure in mice with genetic ablation of a major protein kinase A phosphorylation site in the cardiac ryanodine receptor. *Circ. Res.* 101:819–829. https://doi.org/10.1161/CIRCRESAHA.107.153007

Bers, D.M. 2014. Cardiac sarcoplasmic reticulum calcium leak: Basis and roles in cardiac dysfunction. *Annu. Rev. Physiol.* 76:107–127. https://doi.org/10.1146/annurev-physiol-020911-153308

Cabra, V., T. Murayama, and M. Samsó. 2016. Ultrastructural analysis of self-associated RyR2s. *Biophys. J.* 110:2651–2662. https://doi.org/10.1016/j.bpj.2016.05.013

Cannell, M.B., C.H. Kong, M.S. Imtiaz, and D.R. Laver. 2013. Control of sarcoplasmic reticulum Ca^{2+} release by stochastic RyR gating within a 3D model of the cardiac dyad and importance of induction decay for CICR termination. *Biophys. J.* 104:2149–2159. https://doi.org/10.1016/j.bpj.2013.03.058

Carl, S.L., K. Felix, A.H. Caswell, N.R. Brandt, W.J. Ball Jr., P.L. Vaghy, G. Meissner, and D.G. Ferguson. 1995. Immunolocalization of sarcolemmal dihydropyridine receptor and sarcoplasmic reticular triadin and ryanodine receptor in rabbit ventricle and atrium. *J. Cell Biol.* 129:673–682. https://doi.org/10.1083/jcb.129.3.673

Chelu, M.G., S. Sarma, S. Sood, S. Wang, R.J. van Oort, D.G. Skapura, N. Li, M. Santonastasi, F.U. Müller, W. Schmitz, et al. 2009. Calmodulin kinase II-mediated sarcoplasmic reticulum Ca2+ leak promotes atrial fibrillation in mice. *J. Clin. Invest.* 119:1940–1951. https://doi.org/10.1172/JCI37059

Cheng, H., W.J. Lederer, and M.B. Cannell. 1993. Calcium sparks: Elementary events underlying excitation-contraction coupling in heart muscle. *Science.* 262:740–744. https://doi.org/10.1126/science.8235594

Chiang, D.Y., S. Lahiri, G. Wang, J. Karch, M.C. Wang, S.Y. Jung, A.J.R. Heck, A. Scholten, and X.H.T. Wehrens. 2021. Phosphorylation-dependent

interactome of ryanodine receptor type 2 in the heart. *Proteomes*. 9:27. https://doi.org/10.3390/proteomes9020027
Cross, J.A., and M.P. Dodding. 2019. Motor-cargo adaptors at the organelle-cytoskeleton interface. *Curr. Opin. Cell Biol.* 59:16–23. https://doi.org/10.1016/j.ceb.2019.02.010
Drum, B.M., C. Yuan, A. de la Mata, N. Grainger, and L.F. Santana. 2020. Junctional sarcoplasmic reticulum motility in adult mouse ventricular myocytes. *Am. J. Physiol. Cell Physiol.* 318:C598–C604. https://doi.org/10.1152/ajpcell.00573.2019
Franzini-Armstrong, C. 2018. The relationship between form and function throughout the history of excitation-contraction coupling. *J. Gen. Physiol.* 150:189–210. https://doi.org/10.1085/jgp.201711889
Gaburjakova, J., E. Krejciova, and M. Gaburjakova. 2020. Multisite phosphorylation of the cardiac ryanodine receptor: A random or coordinated event? *Pflugers Arch.* 472:1793–1807. https://doi.org/10.1007/s00424-020-02473-3
Grimm, M., H. Ling, A. Willeford, L. Pereira, C.B. Gray, J.R. Erickson, S. Sarma, J.L. Respress, X.H. Wehrens, D.M. Bers, and J.H. Brown. 2015. CaMKIIδ mediates β-adrenergic effects on RyR2 phosphorylation and SR Ca(2+) leak and the pathophysiological response to chronic β-adrenergic stimulation. *J. Mol. Cell. Cardiol.* 85:282–291. https://doi.org/10.1016/j.yjmcc.2015.06.007
Hayashi, T., M.E. Martone, Z. Yu, A. Thor, M. Doi, M.J. Holst, M.H. Ellisman, and M. Hoshijima. 2009. Three-dimensional electron microscopy reveals new details of membrane systems for Ca2+ signaling in the heart. *J. Cell Sci.* 122:1005–1013. https://doi.org/10.1242/jcs.028175
Holm, S. 1979. A simple sequentially rejective multiple test procedure. *Scand. J. Stat. Theor. Appl.* 6:65–70. https://doi.org/10.2307/4615733
Iaparov, B.I., A.S. Moskvin, I. Zahradník, and A. Zahradníková. 2019. Stochastic and deterministic approaches to modelling calcium release in cardiac myocytes at different spatial arrangements of ryanodine receptors. *Eur. Biophys. J.* 48:579–584. https://doi.org/10.1007/s00249-019-01378-z
Iaparov, B.I., I. Zahradnik, A.S. Moskvin, and A. Zahradníková. 2021. In silico simulations reveal that RYR distribution affects the dynamics of calcium release in cardiac myocytes. *J. Gen. Physiol.* 153:e202012685. https://doi.org/10.1085/jgp.202012685
Katsnelson, A. 2021. Colour me better: Fixing figures for colour blindness. *Nature*. 598:224–225. https://doi.org/10.1038/d41586-021-02696-z
Keefe, J.A., O.M. Moore, K.S. Ho, and X.H.T. Wehrens. 2023. Role of Ca^{2+} in healthy and pathologic cardiac function: From normal excitation-contraction coupling to mutations that cause inherited arrhythmia. *Arch. Toxicol.* 97:73–92. https://doi.org/10.1007/s00204-022-03385-0
Kumari, D., and K. Ray. 2022. Phosphoregulation of kinesins involved in long-range intracellular transport. *Front. Cell Dev. Biol.* 10:873164. https://doi.org/10.3389/fcell.2022.873164
Lanner, J.T., D.K. Georgiou, A.D. Joshi, and S.L. Hamilton. 2010. Ryanodine receptors: Structure, expression, molecular details, and function in calcium release. *Cold Spring Harb. Perspect. Biol.* 2:a003996. https://doi.org/10.1101/cshperspect.a003996
Lavorato, M., T.Q. Huang, V.R. Iyer, S. Perni, G. Meissner, and C. Franzini-Armstrong. 2015. Dyad content is reduced in cardiac myocytes of mice with impaired calmodulin regulation of RyR2. *J. Muscle Res. Cell Motil.* 36:205–214. https://doi.org/10.1007/s10974-015-9405-5
Ling, H., T. Zhang, L. Pereira, C.K. Means, H. Cheng, Y. Gu, N.D. Dalton, K.L. Peterson, J. Chen, D. Bers, and J.H. Brown. 2009. Requirement for Ca^{2+}/calmodulin-dependent kinase II in the transition from pressure overload-induced cardiac hypertrophy to heart failure in mice. *J. Clin. Invest.* 119:1230–1240. https://doi.org/10.1172/JCI38022
Lipp, P., and E. Niggli. 1996. Submicroscopic calcium signals as fundamental events of excitation--contraction coupling in Guinea-pig cardiac myocytes. *J. Physiol.* 492:31–38. https://doi.org/10.1113/jphysiol.1996.sp021286
López-López, J.R., P.S. Shacklock, C.W. Balke, and W.G. Wier. 1994. Local, stochastic release of Ca^{2+} in voltage-clamped rat heart cells: Visualization with confocal microscopy. *J. Physiol.* 480:21–29. https://doi.org/10.1113/jphysiol.1994.sp020337
Marx, S.O., J. Gaburjakova, M. Gaburjakova, C. Henrikson, K. Ondrias, and A.R. Marks. 2001. Coupled gating between cardiac calcium release channels (ryanodine receptors). *Circ. Res.* 88:1151–1158. https://doi.org/10.1161/hh1101.091268
Marx, S.O., S. Reiken, Y. Hisamatsu, T. Jayaraman, D. Burkhoff, N. Rosemblit, and A.R. Marks. 2000. PKA phosphorylation dissociates FKBP12.6 from the calcium release channel (ryanodine receptor): Defective regulation in failing hearts. *Cell.* 101:365–376. https://doi.org/10.1016/S0092-8674(00)80847-8
Meissner, G. 2017. The structural basis of ryanodine receptor ion channel function. *J. Gen. Physiol.* 149:1065–1089. https://doi.org/10.1085/jgp.201711878
Olejnik, S., J. Li, S. Supattathum, and C.J. Huberty. 1997. Multiple testing and statistical power with modified Bonferroni procedures. *J. Educ. Behav. Stat.* 22:389–406. https://doi.org/10.2307/1165229
Peng, W., H. Shen, J. Wu, W. Guo, X. Pan, R. Wang, S.R. Chen, and N. Yan. 2016. Structural basis for the gating mechanism of the type 2 ryanodine receptor RyR2. *Science*. 354:aah5324. https://doi.org/10.1126/science.aah5324
Pereira, L., H. Cheng, D.H. Lao, L. Na, R.J. van Oort, J.H. Brown, X.H. Wehrens, J. Chen, and D.M. Bers. 2013. Epac2 mediates cardiac β1-adrenergic-dependent sarcoplasmic reticulum Ca^{2+} leak and arrhythmia. *Circulation*. 127:913–922. https://doi.org/10.1161/CIRCULATIONAHA.112.148619
Porta, M., P.L. Diaz-Sylvester, J.T. Neumann, A.L. Escobar, S. Fleischer, and J.A. Copello. 2012. Coupled gating of skeletal muscle ryanodine receptors is modulated by Ca^{2+}, Mg^{2+}, and ATP. *Am. J. Physiol. Cell Physiol.* 303:C682–C697. https://doi.org/10.1152/ajpcell.00150.2012
Potenza, D.M., R. Janicek, M. Fernandez-Tenorio, E. Camors, R. Ramos-Mondragón, H.H. Valdivia, and E. Niggli. 2019. Phosphorylation of the ryanodine receptor 2 at serine 2030 is required for a complete β-adrenergic response. *J. Gen. Physiol.* 151:131–145. https://doi.org/10.1085/jgp.201812155
Potenza, D.M., R. Janicek, M. Fernandez-Tenorio, and E. Niggli. 2020. Activation of endogenous protein phosphatase 1 enhances the calcium sensitivity of the ryanodine receptor type 2 in murine ventricular cardiomyocytes. *J. Physiol.* 598:1131–1150. https://doi.org/10.1113/JP278951
Respress, J.L., R.J. van Oort, N. Li, N. Rolim, S.S. Dixit, A. deAlmeida, N. Voigt, W.S. Lawrence, D.G. Skapura, K. Skårdal, et al. 2012. Role of RyR2 phosphorylation at S2814 during heart failure progression. *Circ. Res.* 110:1474–1483. https://doi.org/10.1161/CIRCRESAHA.112.268094
Satoh, H., L.A. Blatter, and D.M. Bers. 1997. Effects of $[Ca^{2+}]i$, SR Ca^{2+} load, and rest on Ca^{2+} spark frequency in ventricular myocytes. *Am. J. Physiol.* 272:H657–H668.
Schindelin, J., I. Arganda-Carreras, E. Frise, V. Kaynig, M. Longair, T. Pietzsch, S. Preibisch, C. Rueden, S. Saalfeld, B. Schmid, et al. 2012. Fiji: An open-source platform for biological-image analysis. *Nat. Methods*. 9:676–682. https://doi.org/10.1038/nmeth.2019
Scholz, F.W., and M.A. Stephens. 1987. K-sample anderson-darling tests. *J. Am. Stat. Assoc.* 82:918–924. https://doi.org/10.2307/2288805
Scriven, D.R., P. Asghari, M.N. Schulson, and E.D. Moore. 2010. Analysis of Cav1.2 and ryanodine receptor clusters in rat ventricular myocytes. *Biophys. J.* 99:3923–3929. https://doi.org/10.1016/j.bpj.2010.11.008
Scriven, D.R.L., A.B. Johnsen, P. Asghari, K.C. Chou, and E.D.W. Moore. 2023. Ryanodine receptor clusters enlarge symmetrically and coalesce afer application of isoproterenol. *J. Gen. Physiol.* 155:e202213109. https://doi.org/10.1085/jgp.202213109
Sikkel, M.B., D.P. Francis, J. Howard, F. Gordon, C. Rowlands, N.S. Peters, A.R. Lyon, S.E. Harding, and K.T. MacLeod. 2017. Hierarchical statistical techniques are necessary to draw reliable conclusions from analysis of isolated cardiomyocyte studies. *Cardiovasc. Res.* 113:1743–1752. https://doi.org/10.1093/cvr/cvx151
Sun, X.H., F. Protasi, M. Takahashi, H. Takeshima, D.G. Ferguson, and C. Franzini-Armstrong. 1995. Molecular architecture of membranes involved in excitation-contraction coupling of cardiac muscle. *J. Cell Biol.* 129:659–671. https://doi.org/10.1083/jcb.129.3.659
Tanskanen, A.J., J.L. Greenstein, A. Chen, S.X. Sun, and R.L. Winslow. 2007. Protein geometry and placement in the cardiac dyad influence macroscopic properties of calcium-induced calcium release. *Biophys. J.* 92:3379–3396. https://doi.org/10.1529/biophysj.106.089425
Uchinoumi, H., Y. Yang, T. Oda, N. Li, K.M. Alsina, J.L. Puglisi, Y. Chen-Izu, R.L. Cornea, X.H.T. Wehrens, and D.M. Bers. 2016. CaMKII-dependent phosphorylation of RyR2 promotes targetable pathological RyR2 conformational shift. *J. Mol. Cell. Cardiol.* 98:62–72. https://doi.org/10.1016/j.yjmcc.2016.06.007
Ullrich, N.D., H.H. Valdivia, and E. Niggli. 2012. PKA phosphorylation of cardiac ryanodine receptor modulates SR luminal Ca^{2+} sensitivity. *J. Mol. Cell. Cardiol.* 53:33–42. https://doi.org/10.1016/j.yjmcc.2012.03.015
van Oort, R.J., M.D. McCauley, S.S. Dixit, L. Pereira, Y. Yang, J.L. Respress, Q. Wang, A.C. De Almeida, D.G. Skapura, M.E. Anderson, et al. 2010. Ryanodine receptor phosphorylation by calcium/calmodulin-dependent protein kinase II promotes life-threatening ventricular arrhythmias in

mice with heart failure. *Circulation*. 122:2669–2679. https://doi.org/10.1161/CIRCULATIONAHA.110.982298

Van Petegem, F. 2015. Ryanodine receptors: Allosteric ion channel giants. *J. Mol. Biol.* 427:31–53. https://doi.org/10.1016/j.jmb.2014.08.004

Vega, A.L., C. Yuan, V.S. Votaw, and L.F. Santana. 2011. Dynamic changes in sarcoplasmic reticulum structure in ventricular myocytes. *J. Biomed. Biotechnol.* 2011:382586. https://doi.org/10.1155/2011/382586

Wehrens, X.H., S.E. Lehnart, S.R. Reiken, and A.R. Marks. 2004. Ca^{2+}/calmodulin-dependent protein kinase II phosphorylation regulates the cardiac ryanodine receptor. *Circ. Res.* 94:e61–e70. https://doi.org/10.1161/01.RES.0000125626.33738.E2

Witcher, D.R., R.J. Kovacs, H. Schulman, D.C. Cefali, and L.R. Jones. 1991. Unique phosphorylation site on the cardiac ryanodine receptor regulates calcium channel activity. *J. Biol. Chem.* 266:11144–11152. https://doi.org/10.1016/S0021-9258(18)99140-4

Xiao, B., M.T. Jiang, M. Zhao, D. Yang, C. Sutherland, F.A. Lai, M.P. Walsh, D.C. Warltier, H. Cheng, and S.R. Chen. 2005. Characterization of a novel PKA phosphorylation site, serine-2030, reveals no PKA hyperphosphorylation of the cardiac ryanodine receptor in canine heart failure. *Circ. Res.* 96:847–855. https://doi.org/10.1161/01.RES.0000163276.26083.e8

Xiao, B., X. Tian, W. Xie, P.P. Jones, S. Cai, X. Wang, D. Jiang, H. Kong, L. Zhang, K. Chen, et al. 2007. Functional consequence of protein kinase A-dependent phosphorylation of the cardiac ryanodine receptor: Sensitization of store overload-induced Ca^{2+} release. *J. Biol. Chem.* 282:30256–30264. https://doi.org/10.1074/jbc.M703510200

Supplemental material

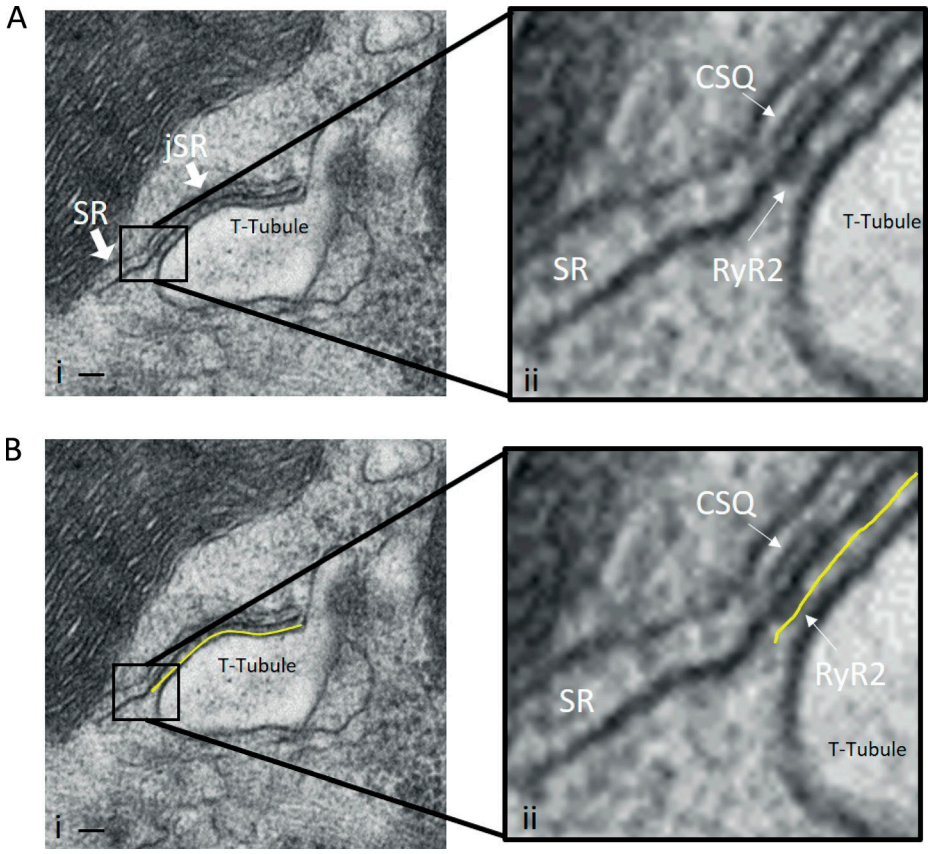

Figure S1. **Measurement of the dyad length.** The lengths of the dyads, regions of close apposition between jSR membranes with either a t-tubule or surface membrane, were measured using Fiji (ImageJ). **(A i)** jSR adjacent to a t-tubule. Extended SR is also visible in this image (SR) and displays neither CSQ in its interior nor RyR2 on its surface. Scale bar = 50 nm. **(B i)** Yellow line displays the length of the jSR. **(A ii and B ii)** Sevenfold magnification of the regions in A i and B i.

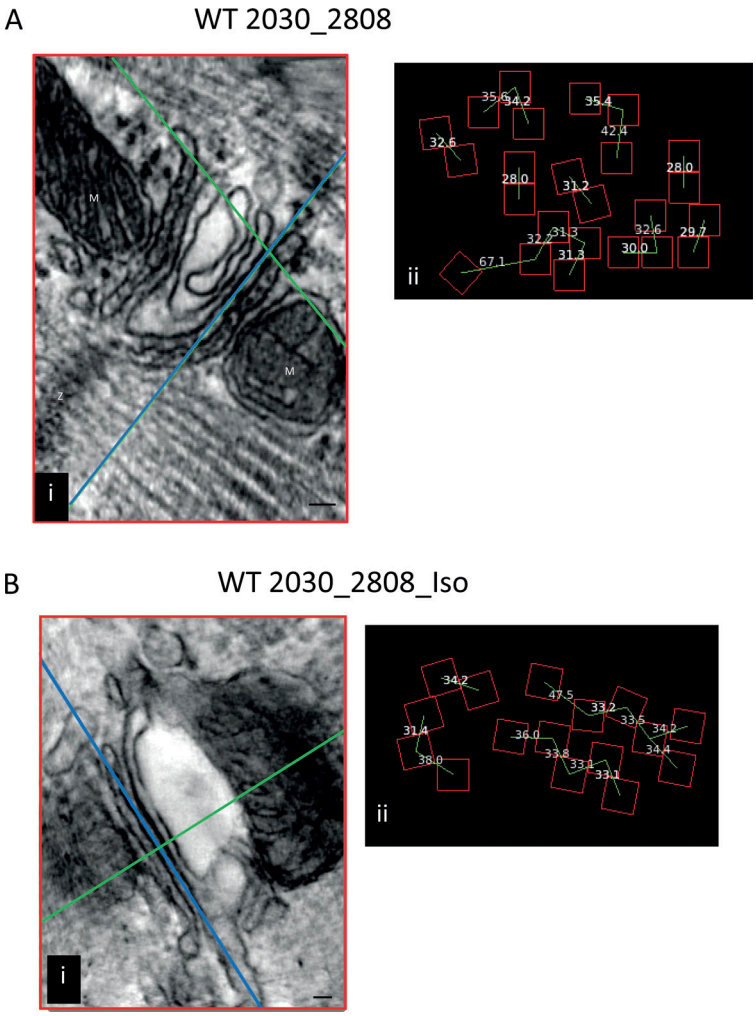

Figure S2. **Tetramer positions and NNDs for WT 2030_2808. (A i)** A single image plane extracted from the dual-tilt tomogram of a mouse left ventricular myocyte fixed in situ. Different orthogonal planes from within the volume of the tomogram are indicated by different colors; XY in red, YZ in green, and XZ in blue. The intersection point of all three planes lies within a single ryanodine receptor and the XZ plane (blue line) was positioned to parallel, as nearly as possible, the jSR membrane, but to be within the cleft and to bisect the ryanodine receptors. Scale bar is 30 nm. **(A ii)** An enlarged view of the tetramer distribution (red boxes, 27 nm^2) and their NNDs. **(B)** Data for mice that had been treated with 300 nmol/liter ISO for 2 min. M, mitochondrion; Z, Z line.

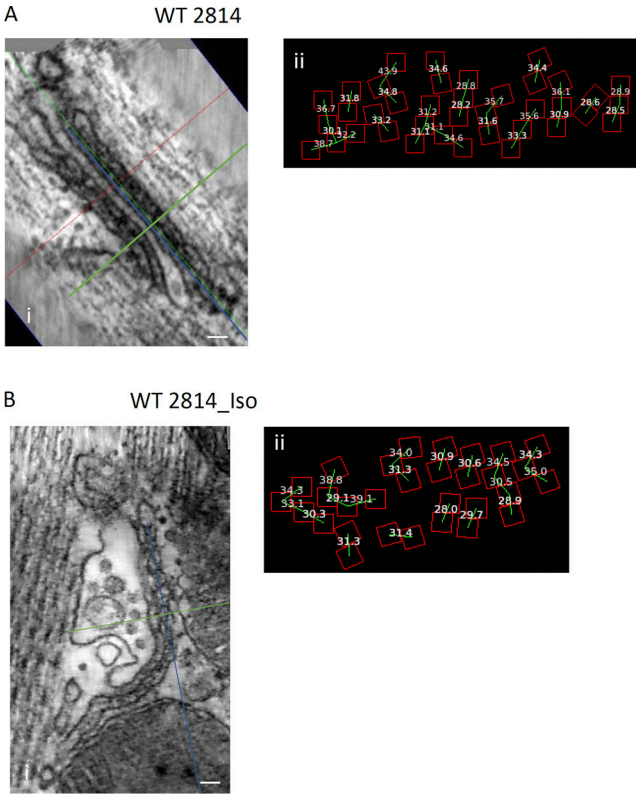

Figure S3. **Tetramer positions and NNDs for WT2814. (A)** Control. **(B)** Iso treated. (i) Dyad cross-section. (ii) Tetramer placement and NND.

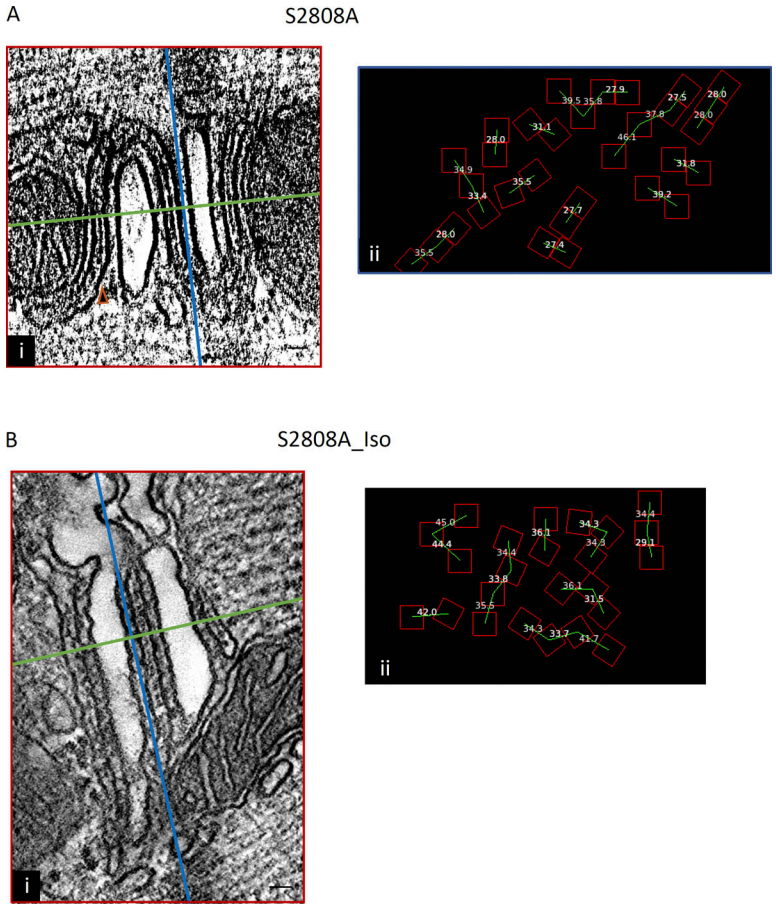

Figure S4. **Tetramer positions and NNDs for S2808A. (A)** Control. **(B)** Iso treated. (i) Dyad cross-section. (ii) Tetramer placement and NND.

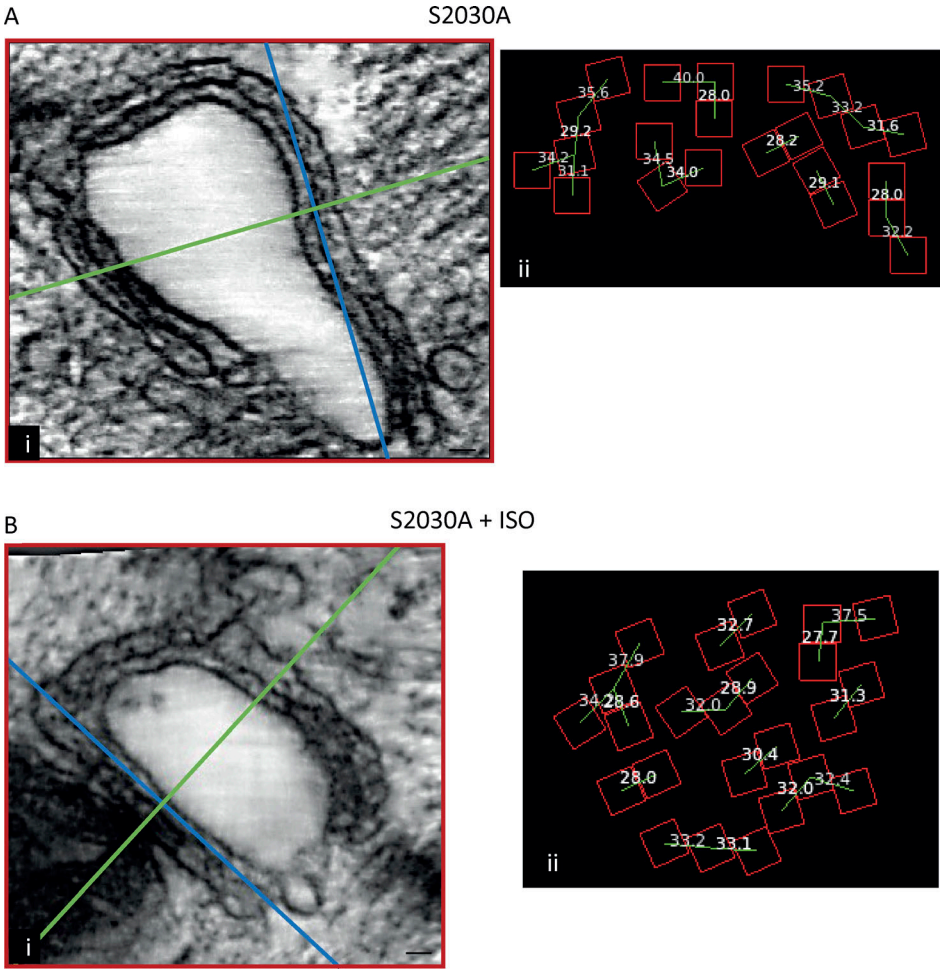

Figure S5. **Tetramer positions and NNDs for S2030A. (A)** Control. **(B)** Iso treated. (i) Dyad cross-section. (ii) Tetramer placement and NND.

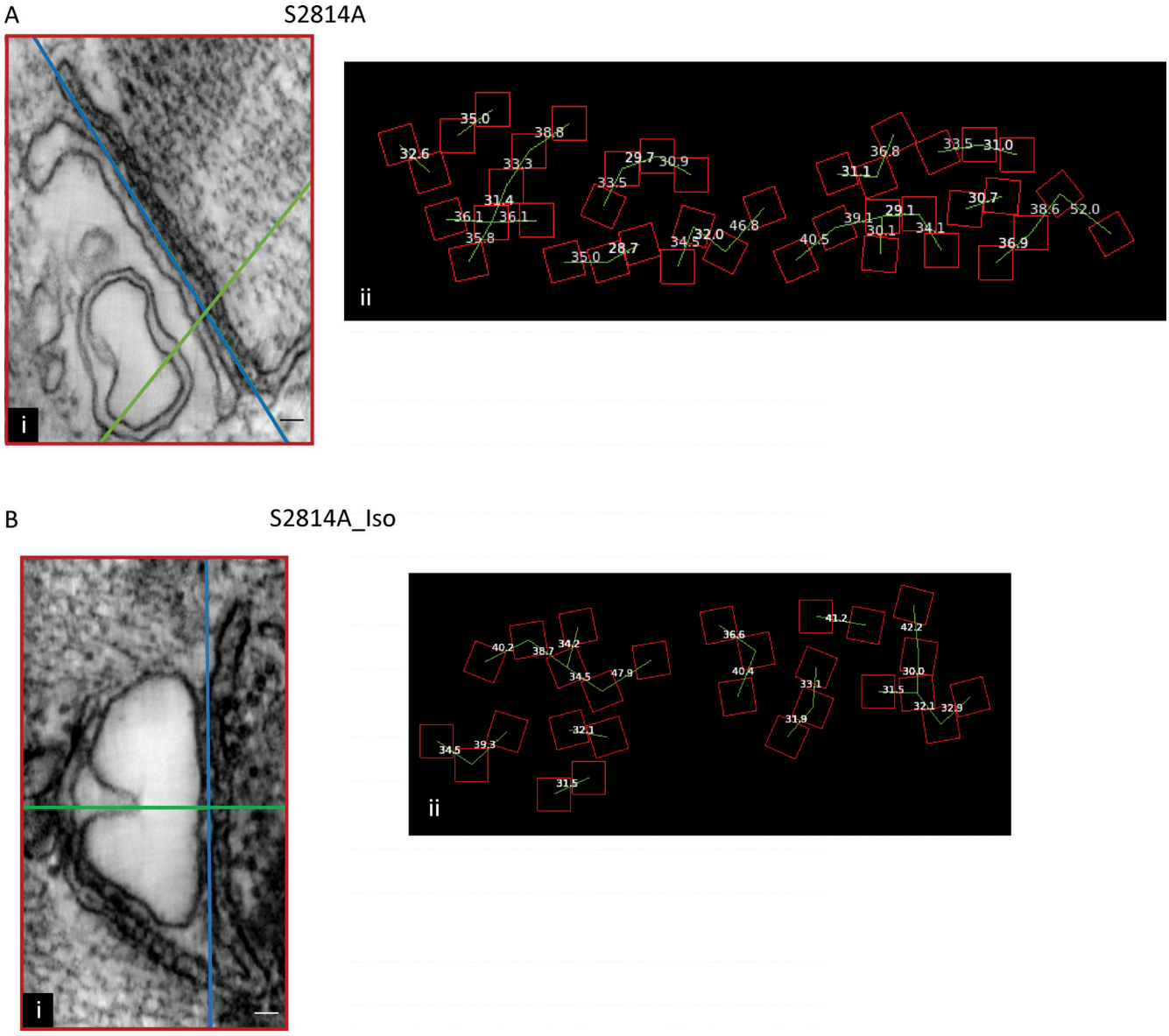

Figure S6. **Tetramer positions and NNDs for S2814A. (A)** Control. **(B)** Iso treated. (i) Dyad cross-section. (ii) Tetramer placement and NND.

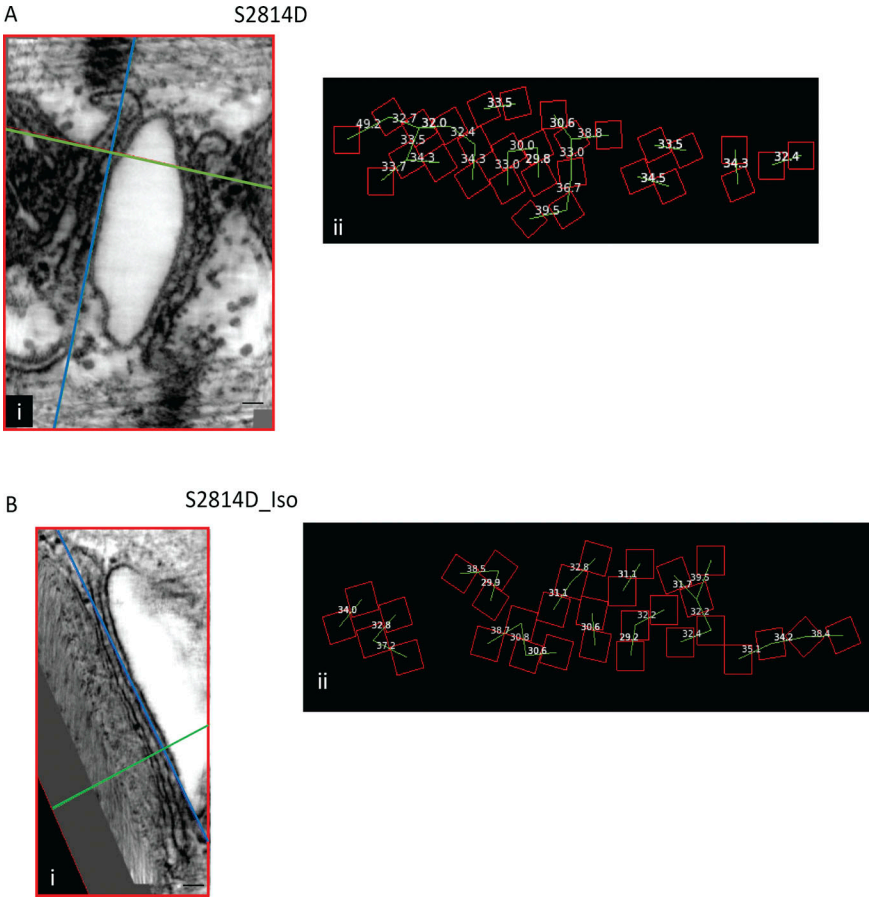

Figure S7. **Tetramer positions and NNDs for S2814D. (A)** Control. **(B)** Iso treated. (i) Dyad cross-section. (ii) Tetramer placement and NND.

Two tables are provided online. Table S1 shows hierarchical data analysis. Table 2 lists the median, first and third quartiles, and minimum and maximum values for the junction lengths for all of the mice.